Aalto University

Majumdar, Sayani; Tan, Hongwei; Pande, Ishan; Van Dijken, Sebastiaan

Crossover from synaptic to neuronal functionalities through carrier concentration control in Nb-doped SrTiO$_3$-based organic ferroelectric tunnel junctions

Crossover from synaptic to neuronal functionalities through carrier concentration control in Nb-doped SrTiO₃-based organic ferroelectric tunnel junctions

Sayani Majumdar [ID], Hongwei Tan [ID], Ishan Pande [ID], and Sebastiaan van Dijken [ID]

COLLECTIONS

Paper published as part of the special topic on Emerging Materials in Neuromorphic Computing
Note: This paper is part of the Special Topic on Emerging Materials in Neuromorphic Computing.

View Online   Export Citation   CrossMark

ARTICLES YOU MAY BE INTERESTED IN

Ferroelectric materials for neuromorphic computing
APL Materials 7, 091109 (2019); https://doi.org/10.1063/1.5108562

Multilevel HfO₂-based RRAM devices for low-power neuromorphic networks
APL Materials 7, 081120 (2019); https://doi.org/10.1063/1.5108650

Metal-insulator transition in (111) SrRuO₃ ultrathin films
APL Materials 7, 091106 (2019); https://doi.org/10.1063/1.5109374

Crossover from synaptic to neuronal functionalities through carrier concentration control in Nb-doped SrTiO₃-based organic ferroelectric tunnel junctions

View Online   Export Citation   CrossMark

Sayani Majumdar,[1,2,a] Hongwei Tan,[2] Ishan Pande,[2] and Sebastiaan van Dijken[2]

AFFILIATIONS

[1] VTT Technical Research Centre of Finland Ltd., P.O. Box 1000, FI-02044 VTT, Finland
[2] Nanospin, Department of Applied Physics, Aalto University School of Science, P.O. Box 15100, FI-00076 Aalto, Finland

Note: This paper is part of the Special Topic on Emerging Materials in Neuromorphic Computing.
[a] E-mail: sayani.majumdar@vtt.fi

ABSTRACT

The development of neuromorphic architectures depends on the engineering of new functional materials and material interfaces. Here, we present a study on organic ferroelectric tunnel junctions (FTJs) comprising a metal/ferroelectric/semiconductor stack with varying charge carrier density in the semiconducting electrode and demonstrate fast, volatile switching behavior when the bound polarization charges in the tunnel barrier are insufficiently screened. The manipulation of ferroelectric polarization and depolarization dynamics in our FTJs through pulse magnitude, duration, and delay time constitutes a controlled transition from synaptic behavior to integrate-and-fire neuronal activity. This ability to tune the response of a single memristor device via charge carrier optimization opens pathways for the design of smart electronic neurons.

Electrically controlled switching of ferroelectric polarization in ferroelectric capacitors has been studied as a promising concept for nonvolatile memories.[1,2] Ferroelectric random access memories (FeRAMs) offering fast writing speeds at low energy costs are already commercially available. However, FeRAMs based on ferroelectric capacitors exhibit destructive readout and, hence, the data need to be rewritten after each reading operation. With the improvement of ultrathin film fabrication techniques, ferroelectric tunnel junctions (FTJs) comprising a nanometer-thick ferroelectric layer sandwiched between two metal electrodes have emerged as a promising candidate for energy efficient resistance switching memories offering nondestructive readout and large scale integration.[3,4] In FTJs, ferroelectric polarization switching in the tunnel barrier produces a modulation of the tunnel barrier height if the Thomas-Fermi screening lengths of the two electrodes differ,[5,6] leading to ON and OFF states of tunneling transport. If one of the metal electrodes in a FTJ is replaced by a semiconductor, an even larger resistance switching effect is measured because of the formation or elimination of an additional Schottky barrier upon ferroelectric switching in the tunnel barrier.[7–10] In Nb-doped SrTiO₃ (NSTO)-based FTJs with a 4 unit-cell-thick BaTiO₃ tunnel barrier, a giant R_{OFF}/R_{ON} ratio of 10^6 has been demonstrated recently.[11] While such large resistance switching effects are promising for resistance memory devices working at room temperature, BaTiO₃ requires high-temperature growth in a vacuum deposition system. Together with the presence of toxic heavy-metal elements, this poses challenges on the integration of this ferroelectric material in practical applications.

Metal-insulator-semiconductor heterostructures are heavily used in the electronics industry because they allow for versatile band engineering. SrTiO₃ has also attracted a lot of interest following the discovery of emergent phenomena at its interface with other complex oxides.[12,13] Semiconducting SrTiO₃, which is obtained by Nb doping at the Ti site, exhibits an unconventional electrical conductivity compared to Si, Ge, and GaAs[14] because of an unusual

dependence of its permittivity on temperature and electric field.[15,16] Although this makes the analysis and modeling of $SrTiO_3$-based systems more complex, it also opens up possibilities for new device physics.

In our previous work, we observed a resistance switching effect of up to 5 orders of magnitude in Au/P(VDF-TrFE)/NSTO FTJs.[17,18] Moreover, reproducible switching between multiple intermediate resistance states, continuous potentiation and depression, long data retention, and spike-timing dependent plasticity (STDP) was demonstrated. Because of these attributes, organic FTJs are a promising candidate for nonvolatile memory elements and electronic synapses in neuromorphic computing architectures. P(VDF-TrFE) is a long-chain copolymer with chemical formula $[(CH_2-CF_2)_n-(CF_2-CHF)_n]$. Since this organic ferroelectric material shows stable ferroelectricity down to 2 monolayers,[19–21] it is a good barrier material for FTJs. In the work presented here, we vary the charge carrier density in the NSTO bottom electrode of organic FTJs to investigate its effect on resistance switching. Our transport measurements indicate a lowering of the polarization retention for weakly doped NSTO electrodes, highlighting a crossover from synaptic to neuronal behavior through a modification of the semiconductor charge density. As an example, we demonstrate that a leaky integrate-and-fire response is produced by FTJs with the lowest Nb doping concentration without any additional electronic circuitry.

The FTJs were prepared by spin coating P(VDF-TrFE) thin films onto NSTO substrates with Nb concentrations of 0.25 wt. %, 0.5 wt. %, and 0.7 wt. %, obtained from Surfacenet GmbH. For spin coating, we prepared a P(VDF-TrFE) solution by dissolving 70:30 copolymer powder from Piezotech in methyl-ethyl ketone (MEK). The solution was spin-coated at 4000 rpm for 1 min followed by annealing in air at $150\,^{\circ}C$ for 2 h. This process resulted in 6-nm-thick P(VDF-TrFE) ferroelectric films, as confirmed by atomic force microscopy measurements (see Fig. S1 of the supplementary

material). Finally, we used electron-beam evaporation to grow 100-nm-thick Au electrodes through a metal shadow mask. The size of the top electrodes was 0.07 mm². A schematic of a FTJ sample is shown in Fig. 1(a). Hereafter, we label the three types of samples as Nb0.25, Nb0.5, and Nb0.7. Electrical transport measurements on FTJs were performed at room temperature. We used a probe station to contact the bottom and top electrodes in a two-point measurement geometry to a Keithley 2400 sourcemeter or Keithley 4200 semiconductor analyzer. Voltage pulses were applied to the junctions using an arbitrary function generator (Tektronix AFG 1062). For capacitance (C)–voltage (V) measurements, we used an impedance analyzer (Novocontrol Alpha-A). C–V curves were measured for frequencies ranging from 1 kHz to 10 MHz using an AC voltage of 1 V and varying DC bias voltages. In all measurements, we grounded the NSTO bottom electrode and applied voltages to one of the Au top contacts.

To investigate the effect of Nb doping on resistance switching in our FTJs, we measured current (I)–voltage (V) curves in a ±4 V range [Figs. 2(a)–2(c)]. In all cases, hysteretic I–V responses with rectifying behavior in the forward and reverse bias directions are obtained. With decreasing Nb doping concentration (from 0.7 wt. % to 0.25 wt. %), the tunneling current in the ON state (I_{ON}) decreases. The current in the OFF state (I_{OFF}) is similar for Nb doping concentrations of 0.7 wt. % and 0.5 wt. %, but it is about 1 order of magnitude smaller for the FTJ with 0.25 wt. % Nb. Resistance (R)–voltage (V_P) curves obtained by applying 100 ms rectangular voltage pulses of varying amplitude (from −4 V to +3 V and back for Nb0.7 and Nb0.5 and from −5 V to +3 V and back for Nb0.25) are shown in Figs. 2(d)–2(f). After each voltage pulse, the junction resistance was measured using a bias voltage of −0.1 V for Nb0.7 and Nb0.5 and +0.4 V for Nb0.25. Higher reading bias was used on Nb0.25 to ensure a good signal-to-noise ratio for this more resistive FTJ. A more than 4 orders of magnitude resistance switching effect is observed for all
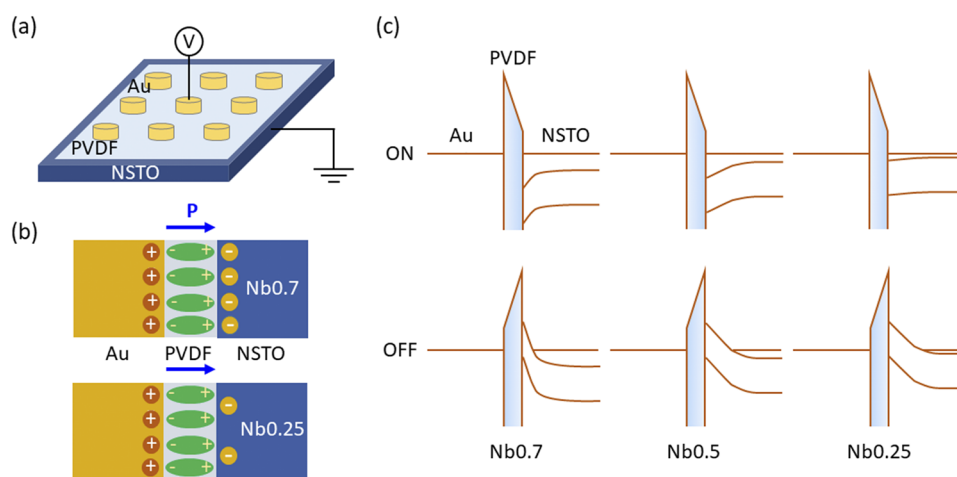
FIG. 1. (a) Schematic of FTJs on a NSTO substrate. (b) Charge distributions in FTJs if the polarization of the P(VDF-TrFE) tunnel barrier points toward the NSTO substrate (ON state). Nearly complete and incomplete screenings of bound polarization charges are illustrated for 0.7 wt.% and 0.25 wt. % Nb doping. (c) Schematic of band alignments in FTJs for the ON and OFF state. If the polarization points away from the NSTO electrode (OFF state, lower panels), electrons in the *n*-type semiconductor deplete from the interface. Consequently, the positively charged immobile donor ions near the interface screen the bound polarization charges in the P(VDF-TrFE) tunnel barrier. This results in the formation of a Schottky barrier. Upon polarization reversal, electrons accumulate near the NSTO interface. This eliminates the Schottky barrier and switches the FTJ to the ON state (upper panels).
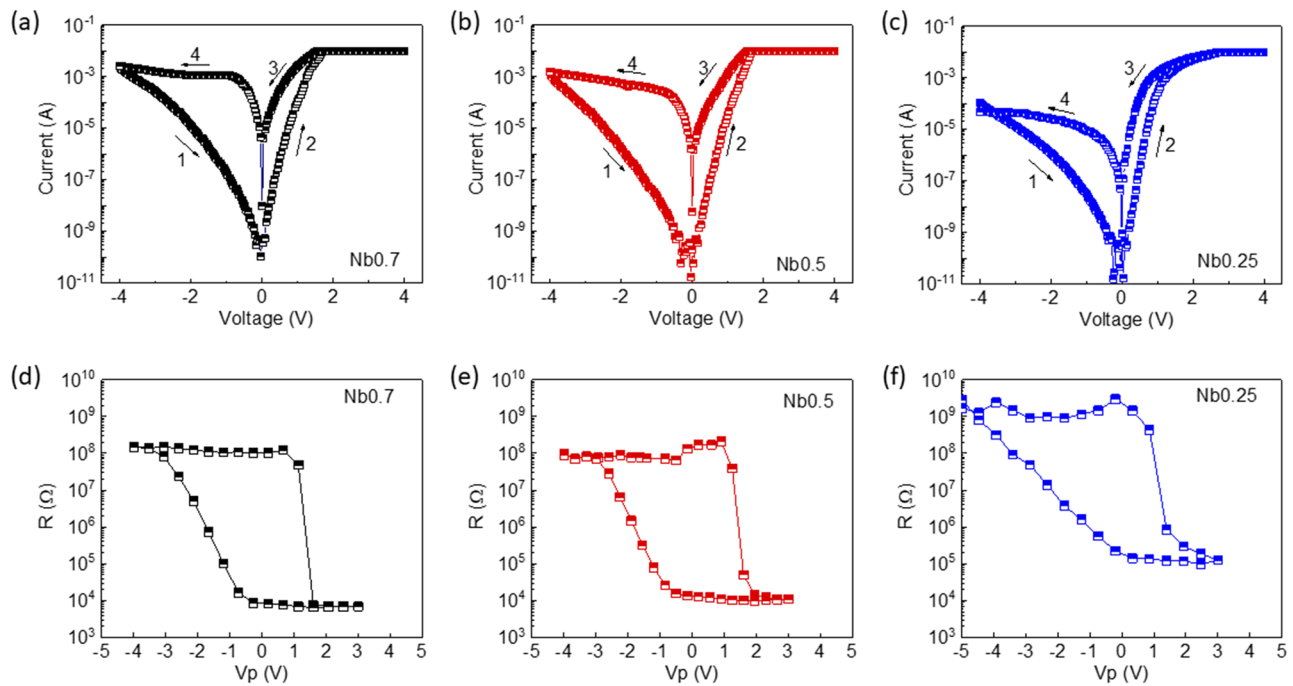
FIG. 2. [(a)–(c)] *I–V* curves of three FTJs with different Nb doping concentrations. [(d)–(f)] *R–V* curves of the same samples for 100 ms writing pulses ranging from −4 V to +3 V for Nb0.7 (d) and Nb0.5 (e) and −5 V to +3 V for Nb0.25 (f). After each voltage pulse, the resistance was read at −0.1 V [(d) and (e)] and +0.4 V (f), respectively.

junctions with almost similar ON and OFF resistances for the Nb0.7 and Nb0.5 samples [Figs. 2(d) and 2(e)]. The resistance values of the Nb0.25 sample are about 1 order of magnitude larger for both the ON and OFF state. Also, the switching voltage increases with decreasing Nb doping concentration. This effect is attributed to an increase in the series resistance across the NSTO substrate, which lowers the electric field across the tunnel barrier at a given voltage.

Resistance switching in metal/ferroelectric/semiconductor Schottky junctions with varying Nb doping concentrations from 0.01 wt. % to 1.0 wt. % has been reported previously for Pt/BaTiO$_3$ (BTO)/NSTO FTJs with a 4 unit-cell-thick BTO tunnel barrier.[11] In that study, the I_{ON}/I_{OFF} ratio was found to improve upon a decrease in the Nb doping concentration down to 0.1 wt. %, which was explained by an optimal electrostatic modulation of the Schottky barrier width at this doping level. Schottky barriers formed by a direct contact between a semiconducting NSTO substrate and a high work-function metal such as Au or Pt also produce a resistance switching effect.[22] The magnitude of the switching effect in these Schottky junctions depends on the quality of the metal-semiconductor interface,[22] which limits the reproducibility and causes device-to-device variations.[23,24] Resistance switching in metal/NSTO devices is often explained by charge trapping at the NSTO interface. Compared to conventional *n*-doped degenerate semiconductors, metal/NSTO Schottky junctions are much more rectifying because the large dielectric permittivity of NSTO (ε_r ≈ 50–300 at room temperature depending on doping concentration) produces a wide depletion region.[25,26] Another interesting feature of NSTO is the dependence of ε_r on electric field.[27] Due to strong

band bending near the metal/NSTO interface, large electric fields up to several MV/cm can develop there.[28] This reduces ε_r and, consequently, leads to an additional narrowing of the depletion layer in an applied bias voltage. In our experiments, we tailor the width of the depletion layer by varying the Nb doping concentration of the NSTO substrate.[29]

After sample fabrication, the polarization of the P(VDF-TrFE) tunnel barrier points away from the NSTO electrode (OFF state). In this case, the electronegative F ions are oriented toward NSTO, causing electrons to deplete from the NSTO interface layer. As a result, the bound polarization charges in the tunnel barrier are screened by positively charged immobile donors in NSTO and a Schottky barrier forms. If a large enough electric field is applied against the polarization direction, the F and H ions start to rotate around the backbone of the P(VDF-TrFE) polymer chain. In saturation, the electropositive H ions and ferroelectric polarization are oriented toward the NSTO electrode. The resulting accumulation of electrons near the NSTO interface eliminates the Schottky barrier and switches the FTJ to the ON state [Figs. 1(b) and 1(c)]. Electrostatic modulations of the Schottky barrier by polarization reversal in the ferroelectric layer are confirmed for all samples by *C–V* measurements (see Fig. S2 of the supplementary material). Together with polarization-induced changes of the tunnel barrier height, the Schottky barrier modulations are responsible for resistance switching in NSTO-based FTJs.[7–10] The Nb doping concentration in the NSTO electrode affects the width of the depletion layer and, thereby, the resistance of the junctions (Fig. 2). Using a simple model, we estimate the width of the depletion layer in NSTO to increase by

about one order of magnitude if the Nb doping concentration is lowered from 0.7 wt. % to 0.25 wt. % (see the supplementary material). We also note that our samples display reproducible resistance switching during consecutive cycles (see Fig. S3 of the supplementary material). Moreover, the maximum variation of the R_{OFF}/R_{ON} ratio between junctions is less than 10%.

Sweeping the voltage between values where the ferroelectric polarization is only partially reversed enables programming of intermediate resistance states [see Figs. S4(a)–S4(c) of the supplementary material]. The FTJs can thus be used as a memristor. Data on the writing of intermediate resistance states using single pulses and the reproducibility of this programming scheme over 1800 writing cycles are plotted in Figs. S4(d)–S4(f) of the supplementary material. We find more reproducible writing of intermediate resistance states for the Nb0.25 sample compared to Nb0.7 and Nb0.5, which we attribute to gradual switching in the latter structures. Previous experiments on NSTO-based FTJs with 1.0 wt. % Nb doping concentration indicate that the writing reproducibility increases for a series of voltage pulses.[18] We expect a similar effect for the Nb0.7 and Nb0.5 samples.

For electronic synaptic devices, long- and short-term potentiation (LTP and STP, respectively) and continuous synaptic weight updates during incessant pulsing are important parameters. Here, we concentrate on STP in our organic FTJs. Figures 3(a)–3(c) summarize data for three Nb doping concentrations. In the experiments, the junctions are first set to the ON state by a single positive voltage pulse. The polarization of the P(VDF-TrFE) tunnel barrier is thus mostly aligned toward the NSTO substrate in this initial state. Subsequently, a series of voltage pulses with a duration of 100 ms and an amplitude of +3 V are applied at an interval of 150 s and the

current is continuously read at small bias. Each voltage pulse aligns the ferroelectric polarization more perpendicular, which increases the current abruptly (potentiation). When the pulse is turned off, the current gradually relaxes toward its initial value. This relaxation effect is explained by the action of a depolarization field that is produced by nonideal screening of bound polarization charges in the ferroelectric tunnel barrier [Fig. 1(b)].[30] The data of Figs. 3(a)–3(c) demonstrate that the time scale of the relaxation process depends on the charge carrier density in the NSTO electrode. By fitting first-order exponential functions to the experimental transport curves, we extract time constants of 75 s for Nb0.7, 40 s for Nb0.5, and 25 s for Nb0.25. We thus observe much faster relaxation to the initial device state for a low Nb doping concentration. This qualitatively agrees with the evolution of the depolarization field, which increases when the charge carrier density in NSTO is too low to efficiently screen the bound polarization charges in the P(VDF-TrFE) tunnel barrier. Model calculations indicate that the strength of the depolarization field in the tunnel barrier of the Nb0.25 sample exceeds that of the Nb0.7 sample by more than a factor of 2 (see the supplementary material).

Figures 3(d)–3(f) show how the FTJ resistance changes during continuous pulsing with 100 negative and 100 positive voltages. The amplitudes of the pulses in these measurements do not suffice to fully reverse the ferroelectric polarization. Instead, small changes in the polarization state produce a gradual depression or potentiation during repeated pulsing, demonstrating reproducible access to a large number of intermediate resistance states.

As demonstrated by the data of Fig. 3, the relaxation of written resistance states depends on the Nb doping level of the NSTO substrate. To assess the effect of Nb doping on resistance
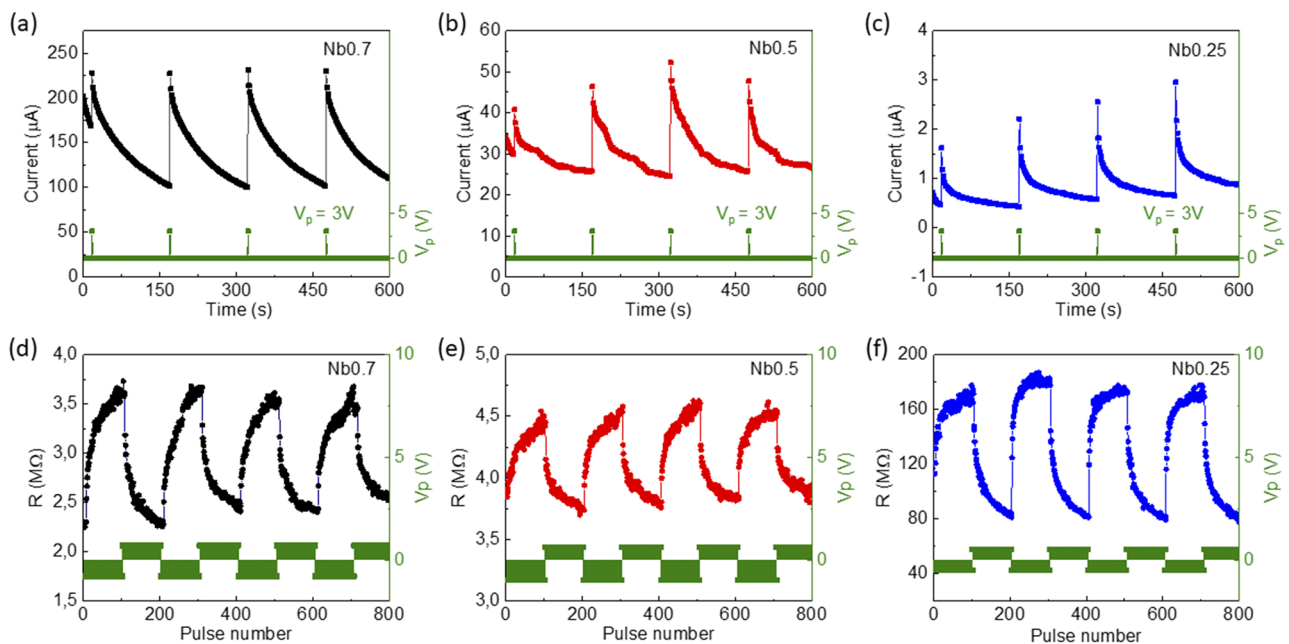
FIG. 3. [(a)–(c)] STP of FTJs with three different Nb doping concentrations. After initialization, single +3 V pulses with a duration of 100 ms are applied at 150 s intervals. The FTJ current is continuously read at a bias voltage of −0.1 V for (a) and (b) and +0.4 V for (c). [(d)–(f)] Evolution of the junction resistance during the application of 100 voltage pulses with alternating polarity. The amplitudes of the pulses are −0.8 V and +0.7 V (d), −1.0 V and +0.6 V (e), and −0.6 V and +0.6 V (f).

switching further, we performed retention tests using a series of 10 pulses to set the initial state [Figs. 4(a)–4(c)]. For the Nb0.7 sample, nearly 80% of the initial R_{OFF}/R_{ON} ratio is maintained after 10^4 s. The resistance states degrade more quickly for the Nb0.5 sample, and the retention is even worse for Nb0.25. These results confirm that a lowering of the Nb doping concentration enhances the volatility of the organic FTJ through an enhancement of the depolarization field.

While the fast dynamic response of the Nb0.25 sample is obviously not suitable for memory functions, it offers a firing-and-recovery type of response that is characteristic of neurons. Before delving further into this potential application, we first assess the behavior of FTJs on shorter time scales. Figures 4(d) and 4(e) compare the potentiation of the tunneling current in Nb0.5 and Nb0.25 samples during the application of 10 ms voltage pulses with increasing amplitude. The duration and time interval between pulses is 100 ms and 1.5 s, respectively. In both samples, the current increases during the pulse sequence, but the accumulative effect is much smaller for the FTJ with 0.25 wt. % Nb because of faster relaxation between consecutive pulses. The dynamic response of the Nb0.25 sample to short voltage pulses is further illustrated by the data of Fig. 4(f) showing measurements of the tunneling current during the application of 10 ms voltage pulses. The changes in the FTJ current are nearly instantaneous on this time scale. We note that the current between pulses evolves differently in Figs. 4(e) and 4(f) because a reading voltage of +0.4 V is continuously used in (e), while no voltage is applied between pulses in (f).

In neural networks, the synapses are responsible for memory and learning through synaptic weight modifications, while the neurons integrate the event-based action potentials and fire when a threshold is reached. Key properties of an electronic neuron are leaky integration, a fire threshold, and fast recovery. In earlier works, memristive devices with additional circuitry were used to produce the required firing response above threshold. For instance, Mott memristors based on a NbO_x layer undergoing a metal-insulator transition as a result of local Joule heating together with a R-C circuit for control of the firing frequency were reported by Pickett et al.[31] and neuron devices using other Mott insulators such as lacunar spinel compounds were investigated by Stoilar et al.[32] Moreover, phase-change neurons[33] and neurons based on conductive Ag filament formation[34] were demonstrated recently. In all these realizations, additional resistors and/or capacitors are used to mimic the firing behavior of a neuron. Next, we will show that our organic FTJs with a limited charge carrier density in the bottom NSTO electrode exhibit neuronlike integrate-and-fire characteristics and self recovery without additional circuitry.

Figure 5(a) shows the current output of a FTJ with 0.25 wt. % Nb in the NSTO electrode when +0.7 V pulses with a duration of 5 ms are applied at a time interval of 100 ms. If the initial state of the FTJ is set close to the OFF state, the output consists of bundles of current spikes with a width of approximately 300 ms and a frequency of 2.2 Hz. The +0.7 V pulses are below threshold, and consequently, the system needs to integrate the effect of several pulses before triggering a response. If the pulse amplitude is enhanced to +0.8 V [Fig. 5(b)], the width of the current pulse bundles increases and their frequency decreases. The width and frequency of the current pulse bundles also depend on the duration of the individual voltage pulses, as
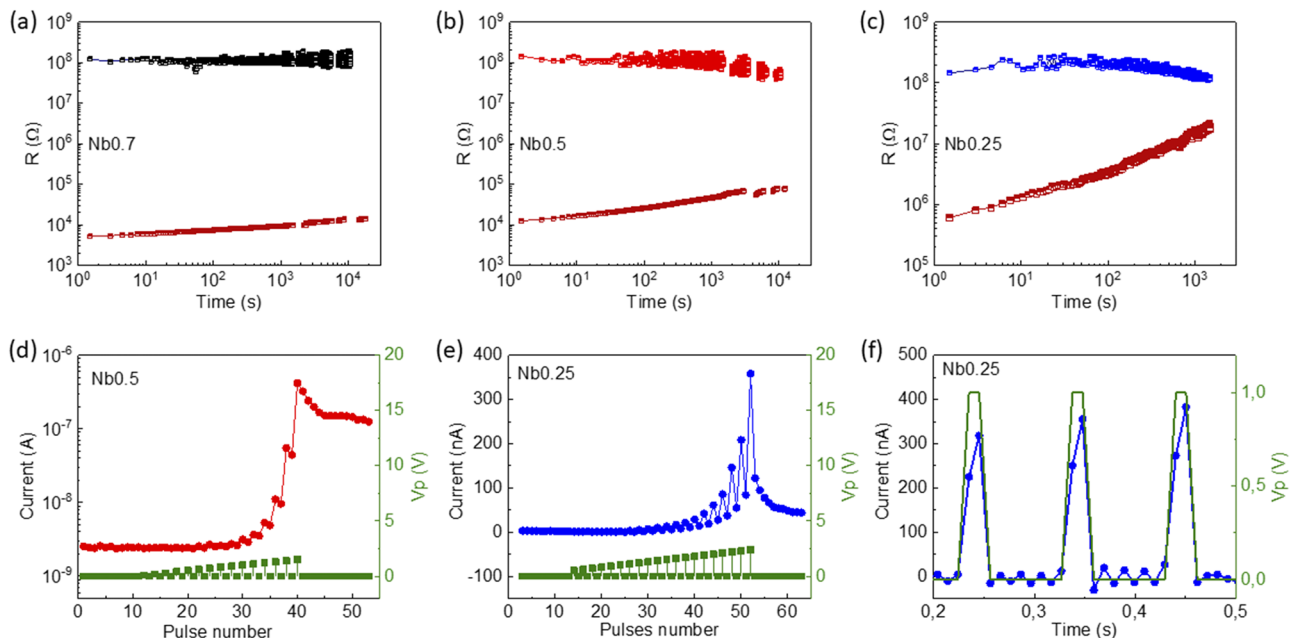

FIG. 4. [(a)–(c)] Resistance retention of FTJs with three different Nb doping concentrations. The initial resistance states are written by a series of 10 pulses with an amplitude of −3 V (OFF state) or +3 V (ON state), and the resistance states are monitored continuously at a reading voltage of −0.1 V [(a) and (b)] and +0.4 V (c). [(d) and (e)] Current response of FTJs with 0.5 wt. % and 0.25 wt. % Nb to 100 ms voltage pulses with increasing amplitude. The interval between voltage pulses is 1.5 s. The currents in (d) and (e) are measured at −0.1 V and +0.4 V, respectively. (f) Current of a Nb0.25 junction during the application of 10 ms voltage pulses with an amplitude of +1.0 V.
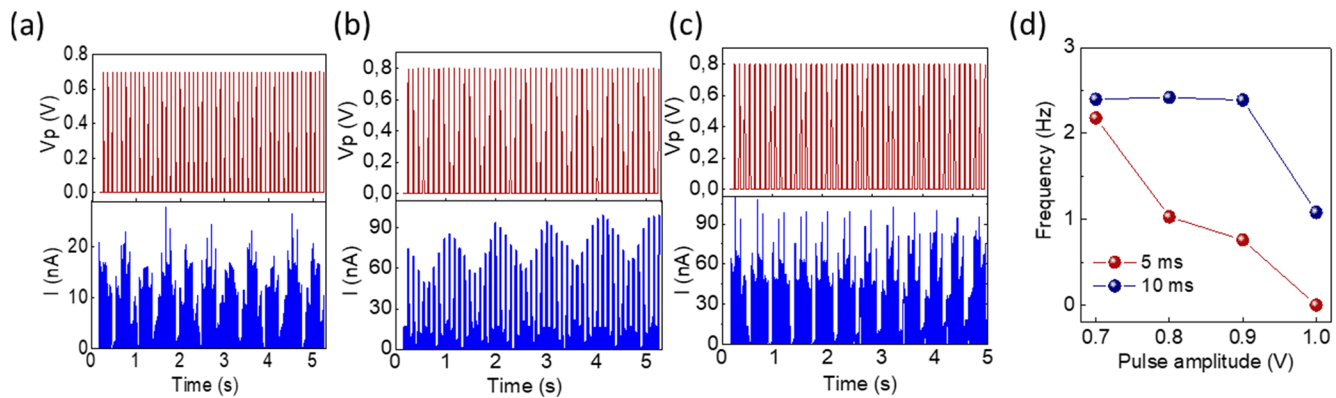
FIG. 5. Oscillatory output current of a FTJ with a Nb doping concentration of 0.25 wt. %. The junction is operated near the OFF state by continuous pulsing with 100 ms intervals. The voltage pulse amplitude and duration are +0.7 V and 5 ms (a), +0.8 V and 5 ms (b), and +0.8 V and 10 ms (c). (d) Frequency of the current pulse bundles as a function of voltage pulse amplitude for 5 ms and 10 ms pulses.

illustrated by Fig. 5(c). All parameters in this measurement are identical to those of Fig. 5(b) except for the pulse duration which was set to 10 ms instead of 5 ms. Obviously, an increase in the pulse duration enhances the frequency of the current pulse bundles. Figure 5(d) summarizes the measured output frequency for two pulse durations and four pulse amplitudes. For a pulse amplitude of +1.0 V, 5 ms pulses with an interval of 100 ms do no longer generate an oscillating output current.

The current oscillations in Figs. 5(a)–5(c) are relatively small, i.e., the FTJ remains close to the OFF state throughout the measurement sequence. A more pronounced integrate-and-fire type of response is produced by longer voltage pulses. Figure 6(a) shows an example for voltage pulses with an amplitude of +1.0 V and a duration of 200 ms. The interval between pulses is about 800 ms. For these parameters, only a small oscillatory response is measured initially. After about 30 s, however, the tunneling current suddenly increases, mimicking the integrate-and-fire behavior of a neuron.[35] The first firing event marks threshold switching from a nearly OFF state to an ON state. The ratio of the first current spike during firing and the current during the last integration pulse is approximately 25. After this, the firing amplitude decreases gradually to a more intermediate level. The integration time required for threshold firing can be set by changing the voltage amplitude and frequency of the continuous pulse train. For instance, Fig. 6(b) shows the integrate-and-fire response for identical pulse parameters as in Fig. 6(a) except for a higher frequency of 2.3 Hz. In this case, the integration time is reduced to 14 s. Another example, shown in Fig. 6(c), indicates a further decrease in the integration time to 5.5 s for voltage pulses with an amplitude of +1.1 V. Besides offering control over the integration time, the pulse parameters also affect relaxation of the tunneling current after the firing event. Based on the measurements of Fig. 6, we conclude that stronger and more frequent pulsing prolong the relaxation time.

Because firing and recovery in our FTJs depend on the dynamics of ferroelectric polarization *and* the strength of the depolarization field, the response is affected not only by pulse amplitude, duration, or frequency (polarization dynamics) but also by sample design. The depolarization field depends on the Nb doping concentration in the NSTO electrode and the thickness of the ferroelectric tunnel barrier. Future studies can make use of these dependencies to further tailor the performance of artificial neurons. Importantly, the results of Figs. 5 and 6 in this paper demonstrate that neuronlike
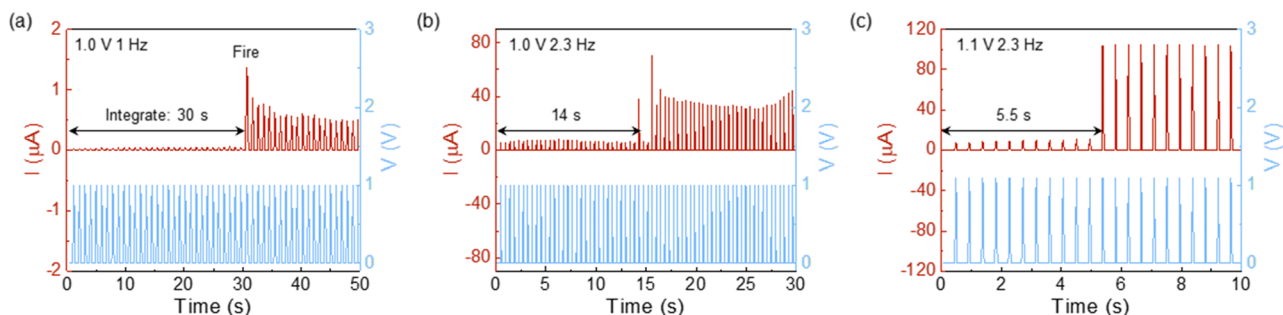

FIG. 6. Emulation of integrate-and-fire behavior using a FTJ with a Nb doping concentration of 0.25 wt. %. The junction is initialized near the OFF state. (a) Continuous pulsing with 200 ms + 1.0 V pulses at a frequency of 1 Hz produces a sudden increase in the tunneling current after 30 s. (b) The integration time before the first firing event decreases to 14 s if the pulse frequency is set to 2.3 Hz. (c) An additional increase in the pulse amplitude to +1.1 V lowers the integration time to 5.5 s.
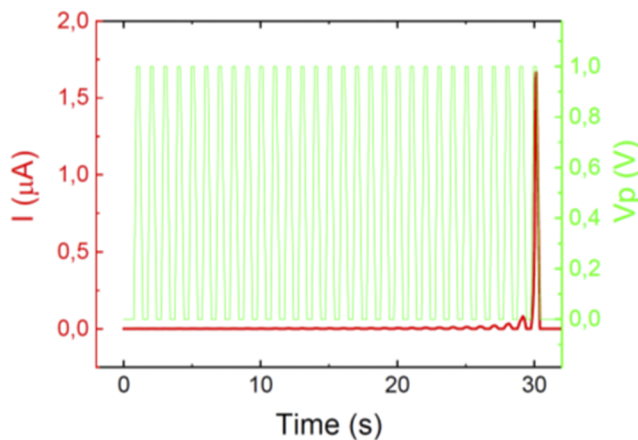
FIG. 7. LTspice simulations of a FTJ replicating the integrate-and-fire response with 200 ms + 1.0 V pulses with an interval of 1 s. Other input parameters are R_{init} = 10^9 Ω, R_{ON} = 6×10^5 Ω, R_{OFF} = 10^9 Ω, and p = 0.1.

firing can be emulated by a single FTJ memristor without additional circuitry.

To understand the dynamic response of our organic FTJs in a more comprehensive way, we performed circuit simulations using LTspice software.[36] Previously, similar computer models have been successfully implemented to simulate the behavior of the first memristor developed by HP labs.[37–39] Operation of the HP memristor is based on oxygen vacancy transport in a TiO_2 layer with doped (R_{ON}) and undoped (R_{OFF}) regions. In the model, the total resistance is written as the weighted sum $R_{MEM} = R_{ON}x + R_{OFF}(1 - x)$, where x is the relative size of the vacancy containing region. Resistance switching in our organic FTJs originates from polarization reversal in the P(VDF-TrFE) tunnel barrier, which proceeds via the nucleation and growth of inverse domains.[18] At intermediate resistances, both domain types are present in the tunnel barrier and areas with polarization pointing toward and away from the NSTO substrate represent R_{ON} and R_{OFF}, respectively. To take boundary effects into account, we employed the window function $f(x) = 1 - (2x - 1)^{2p}$ from Ref. 39 in the simulations. If we set $p = 0.1$, $R_{ON} = 6 \times 10^5$ Ω, $R_{OFF} = 10^9$ Ω, and the initial resistance $R_{init} = R_{OFF} = 10^9$ Ω, we find that an integrate-and-fire response is replicated for a pulse sequence similar to the one used in the experiments of Fig. 6 (see Fig. 7). Moreover, a small oscillatory current is simulated in the integration phase, which also agrees with the experimental observations. Firing after 30 s switches the junction from the OFF state to a near ON state.

Finally, we note that the experiments were conducted with voltage pulses ranging from 5 ms to 100 ms. Our organic FTJs, however, can be operated on much faster time scales.[18] Results on resistance switching using voltage pulses down to 20 ns are shown in Fig. S5 of the supplementary material. The ability to operate FTJ memristors on time scales spanning many orders of magnitude offers great flexibility in the design of neuronal responses. In addition, a reduction in the pulse duration down to nanoseconds drastically reduces the energy consumption per firing event.

In conclusion, we have shown that Nb-doped STO-based organic FTJs exhibit a transition from synapse-type responses

(0.7 wt.% and 0.5 wt.% Nb) to neuronlike behavior (0.25 wt.% Nb). The fast relaxation of resistance states in junctions with a low Nb doping concentration is caused by incomplete screening of the bound polarization charges in the ferroelectric tunnel barrier. Oscillatory current and integrate-and-fire responses are emulated without additional circuitry by variation of the pulse parameters. For FTJs on more conventional semiconductors, a similar neuronlike response is expected, opening a route toward the realization of CMOS compatible electronic neurons for large-scale neuromorphic circuits.

See supplementary material for data regarding device reproducibility, capacitance measurements, device endurance, switching time scale, and calculation of depolarizing field.

REFERENCES

[1] J. F. Scott, Science **315**, 954 (2007).

[2] M. Dawber, K. M. Rabe, and J. F. Scott, Rev. Mod. Phys. **77**, 1083 (2005).

[3] V. Garcia and M. Bibes, Nat. Commun. **5**, 4289 (2014).

[4] A. Gruverman, D. Wu, H. Lu, Y. Wang, H. W. Jang, C. M. Folkman, M. Y. Zhuravlev, D. Felker, M. Rzchowski, C.-B. Eom, and E. Y. Tsymbal, Nano Lett. **9**, 3539 (2009).

[5] M. Zhuravlev, R. Sabirianov, S. Jaswal, and E. Tsymbal, Phys. Rev. Lett. **94**, 246802 (2005).

[6] H. Kohlstedt, N. Pertsev, J. Rodríguez Contreras, and R. Waser, Phys. Rev. B **72**, 125341 (2005).

[7] Z. Wen, C. Li, D. Wu, A. Li, and N. Ming, Nat. Mater. **12**, 617 (2013).

[8] W. J. Hu, Z. Wang, W. Yu, and T. Wu, Nat. Commun. **7**, 10808 (2016).

[9] Z. Hu, Q. Li, M. Li, Q. Wang, Y. Zhu, X. Liu, X. Zhao, Y. Liu, and S. Dong, Appl. Phys. Lett. **102**, 102901 (2013).

[10] X. Wang, B. Song, L. L. Tao, J. Wen, L. Zhang, Y. Zhang, Z. Lv, J. Tang, Y. Sui, B. Song, and X. F. Han, Appl. Phys. Lett. **109**, 163501 (2016).

[11] Z. Xi, J. Ruan, C. Li, C. Zheng, Z. Wen, J. Dai, A. Li, and D. Wu, Nat. Commun. **8**, 15217 (2017).

[12] H. Y. Hwang, Y. Iwasa, M. Kawasaki, B. Keimer, N. Nagaosa, and Y. Tokura, Nat. Mater. **11**, 103 (2012).

[13] J. Mannhart and D. G. Schlom, Science **327**, 1607 (2010).

[14] A. Spinelli, M. A. Torija, C. Liu, C. Jan, and C. Leighton, Phys. Rev. B **81**, 155110 (2010).

[15] T. Susaki, Y. Kozuka, Y. Tateyama, and H. Y. Hwang, Phys. Rev. B **76**, 155110 (2007).

[16] R. A. van der Berg, P. W. M. Blom, J. F. M. Cillessen, and R. M. Wolf, Appl. Phys. Lett. **66**, 697 (1995).

[17] S. Majumdar, B. Chen, Q. H. Qin, H. S. Majumdar, and S. van Dijken, Adv. Funct. Mater. **28**, 1703273 (2018).

[18] S. Majumdar, H. Tan, Q. H. Qin, and S. van Dijken, Adv. Electron. Mater. **5**, 1800795 (2019).

[19] A. V. Bune, V. M. Fridkin, S. Ducharme, L. M. Blinov, S. P. Palto, A. V. Sorokin, S. G. Yudin, and A. Zlatkin, Nature **391**, 874 (1998).

[20] H. Qu, W. Yao, T. Garcia, and J. Zhang, Appl. Phys. Lett. **82**, 4322 (2003).

[21] J. Choi, G. S. Khara, Y. Song, and Y. Zhao, Chem. Phys. Lett. **410**, 339 (2005).

[22] E. Mikheev, B. D. Hoskins, D. B. Strukov, and S. Stemmer, Nat. Commun. **5**, 3990 (2014).

[23] H.-S. Wong, H.-Y. Lee, S. Yu, Y.-S. Chen, Y. Wu, P.-S. Chen, B. Lee, F. Chen, and M.-J. Tsai, Proc. IEEE **100**, 1951 (2012).

[24] J. J. Yang, D. B. Strukov, and D. R. Stewart, Nat. Nanotechnol. **8**, 13 (2013).

[25] B. C. Min, J. C. Lodder, R. Jansen, and K. Motohashi, J. Appl. Phys. **99**, 08S701 (2006).

[26] T. Uhrmann, T. Dimopoulos, A. Kovacs, A. Kohn, S. Weyers, U. Paschen, J. Smoliner, and H. Brckl, J. Phys. D: Appl. Phys. **42**, 145114 (2009).

[27] R. C. Neville, B. Hoeneisen, and C. A. Mead, J. Appl. Phys. **43**, 2124 (1972).

[28] S. Suzuki, T. Yamamoto, H. Suzuki, K. Kawaguchi, K. Takahashi, and Y. Yoshisato, J. Appl. Phys. **81**, 6830 (1997).

[29] S. M. Sze, *Physics of Semiconductor Devices* (John Wiley & Sons, 1981).

[30] R. R. Mehta, S. D. Silverman, and J. T. Jacobs, J. Appl. Phys. **44**, 3379 (1973).

[31] M. D. Pickett, G. M. Ribeiro, and R. S. Williams, Nat. Mater. **12**, 114 (2013).

[32] P. Stoliar, J. Tranchant, B. Corraze, E. Janod, M.-P. Besland, F. Tesler, M. Rozenberg, and L. Cario, Adv. Funct. Mater. **27**, 1604740 (2017).

[33] T. Tuma, A. Pantazi, M. Gallo, A. Sebastian, and E. Eleftheriou, Nat. Nanotechnol. **11**, 693 (2016).

[34] Y. Zhang, W. He, Y. Wu, K. Huang, Y. Shen, J. Su, Y. Wang, Z. Zhang, X. Ji, G. Li, H. Zhang, S. Song, H. Li, L. Sun, R. Zhao, and L. Shi, Small **14**, 1802188 (2018).

[35] G. Indiveri, B. Linares-Barranco, T. J. Hamilton, A. van Schaik, R. Etienne-Cummings, T. Delbruck, S. C. Liu, P. Dudek, P. Häfliger, S. Renaud, J. Schemmel, G. Cauwenberghs, J. Arthur, K. Hynna, F. Folowosele, S. Saighi, T. Serrano-Gotarredona, J. Wijekoon, Y. Wang, and K. G. Boahen, Front. Neurosci. **5**, 73 (2011).

[36] See https://www.analog.com/en/design-center/design-tools-and-calculators/ltspice-simulator.html for LTspice software.

[37] D. B. Strukov, G. S. Snider, D. R. Stewart, and R. S. Williams, Nature **453**, 80 (2008).

[38] Z. Biolek, D. Biolek, and V. Biolkova, Radioengineering **18**, 210 (2009).

[39] Y. N. Joglekar and S. J. Wolf, Eur. J. Phys. **30**, 661 (2009).